Science Advances
AAAS

advances.sciencemag.org/cgi/content/full/4/10/eaat8237/DC1

Supplementary Materials for

Quantum interference mediated vertical molecular tunneling transistors

Chuancheng Jia, Marjan Famili, Marco Carlotti, Yuan Liu, Peiqi Wang, Iain M. Grace, Ziying Feng, Yiliu Wang, Zipeng Zhao, Mengning Ding, Xiang Xu, Chen Wang, Sung-Joon Lee, Yu Huang, Ryan C. Chiechi, Colin J. Lambert*, Xiangfeng Duan*

*Corresponding author. Email: xduan@chem.ucla.edu (X.D.); c.lambert@lancaster.ac.uk (C.J.L.)

Published 12 October 2018, *Sci. Adv.* **4**, eaat8237 (2018)
DOI: 10.1126/sciadv.aat8237

This PDF file includes:

Section S1. Supplementary for device fabrication

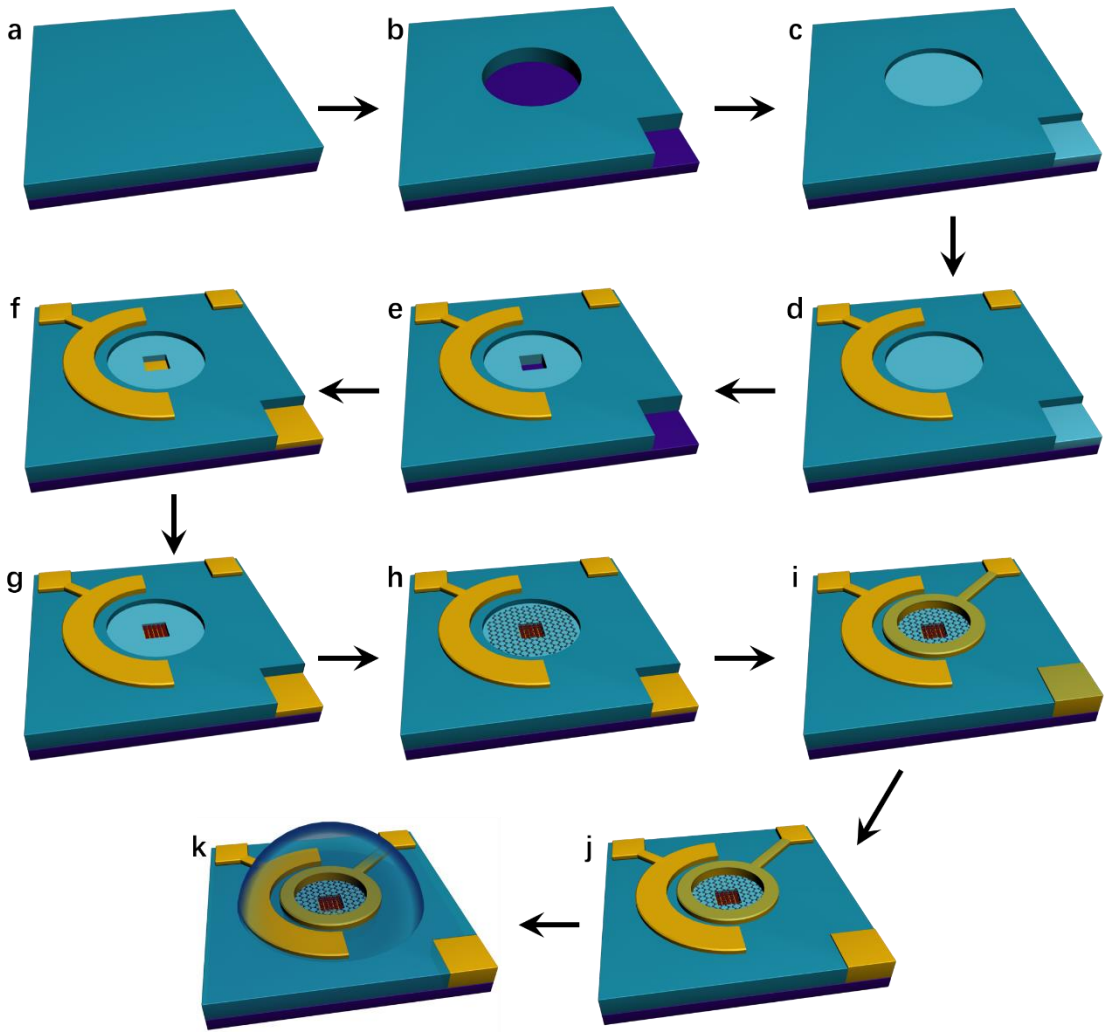

Fig. S1. Fabrication procedure for the vertical molecular transistor. (**A**) Cleaned silicon wafer with proper size. (**B**) Etch the 300 nm SiO_2 layer in the photolithographically patterned 80 μm hole. (**C**) Grow 30 nm SiO_2 by thermally oxidizing. (**D**) Evaporate metal marks and gate electrode. (**E**) Etch for 1.5 μm square holes at 30 nm SiO_2 layer. (**F**) Evaporate ultra-flat Ti/Au (5/23 nm) thin film into the small holes. (**G**) Assemble monolayer molecules on the surface of Au film. (**H**) Transfer and pattern CVD-grown single layer graphene on SAMs. (**I**) Evaporate source and drain electrodes and Al_2O_3 protection layer. (**J**) Remove the Al_2O_3 layer on drain electrode at the corner. (J) Add a drop of diethylmethyl(2-methoxyethyl)ammonium bis(trifluoromethylsulfonyl)imide (DEME-TFSI) ion liquid on the device.

Section S2. Characterization of the devices

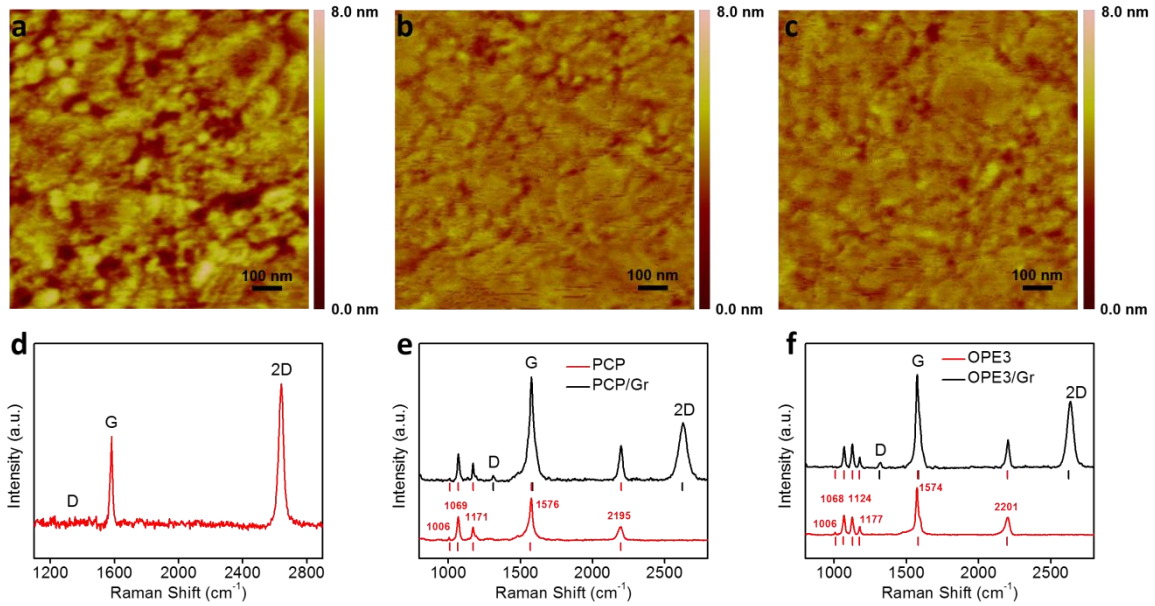

Fig. S2. AFM and Raman characterizations. (**A-C**) AFM images of Ti/Au (5/23 nm) thin films without SAM (A), with PCP SAM (B) and with OPE3 SAM (C). (**D**) Raman spectra of the used graphene. (**E**) Surface enhanced Raman spectra for Au/PCP (red line) and Au/PCP/graphene (black line). (**F**) Surface enhanced Raman spectra for Au/OPE3 (red line) and Au/OPE3/graphene (black line).

The ultra-flat Ti/Au (5/23 nm) thin film (fig. S2a), which works as base layer for the molecules, has a root mean square (RMS) roughness of ~0.89 nm. The PCP sample (fig. S2b) has an RMS roughness of ~0.39 nm. The OPE3 sample (fig. S2c) has an RMS roughness of ~0.41 nm. For PCP and OPE3 samples, the 'smoothing' of the Au film surface indicates the presence of a monolayer. As PCP and OPE3 SAMs have ultra-flat surfaces with RMS roughness of ~0.4 nm and similar molecular lengths of ~2 nm, these ensure the PCP and OPE3 molecules have similar close contact with top graphene layer.

For Raman of the used graphene (fig. S2d), single narrow symmetric 2D peak (≈2706 cm^{-1}), small G/2D ratio, and negligible D peak indicate that single layer graphene with high quality was used. For Raman of PCP (fig. S2e, red line), the peak at 1006 cm^{-1} represents the in-plane ring-breathing mode; the peak at 1069 cm^{-1} represents the in-plane C-H bend; the peak at 1171 cm^{-1} represents the C-S stretching mode coupled with the in-plane ring-breathing mode; the peak at 1576 cm^{-1} comes from phenyl (C=C); the peak at 2195 cm^{-1} comes from alkynyl (C≡C). For Raman of OPE3 (fig. S2f, red line), the peak at 1006 cm^{-1} represents the in-plane ring-breathing mode; the peak at 1068 cm^{-1} represents the in-plane C-H bend; the peaks at 1124, 1177 cm^{-1} represent the C-S stretching mode coupled with the in-plane ring-breathing mode; the peak at 1574 cm^{-1} comes from phenyl (C=C); the peak at 2201 cm^{-1} comes from alkynyl (C≡C). These

Raman characteristics indicate that PCP and OPE3 molecules are successfully self-assembled on Au film. For PCP and OPE3 SAMs covered with graphene layer (fig. S2e,f, black lines), the superposition of Raman peaks of corresponding molecules and graphene can be observed. Besides, enhanced intensities of molecular peaks can be observed for SAM/Gr samples. For instance, the peak intensities at 1069 cm^{-1} and 2195 cm^{-1} for PCP/Gr are ~1.12 times and ~2.54 times of that for PCP (fig. S2e); the peak intensities at 1068 cm^{-1} and 2201 cm^{-1} for OPE3/Gr are ~1.07 times and ~1.57 times of that for OPE3 (fig. S2f). Such graphene enhanced Raman signals for molecules in SAM/Gr samples indicate that the deposition of the top graphene electrode has some effect on the arrangement of molecules.

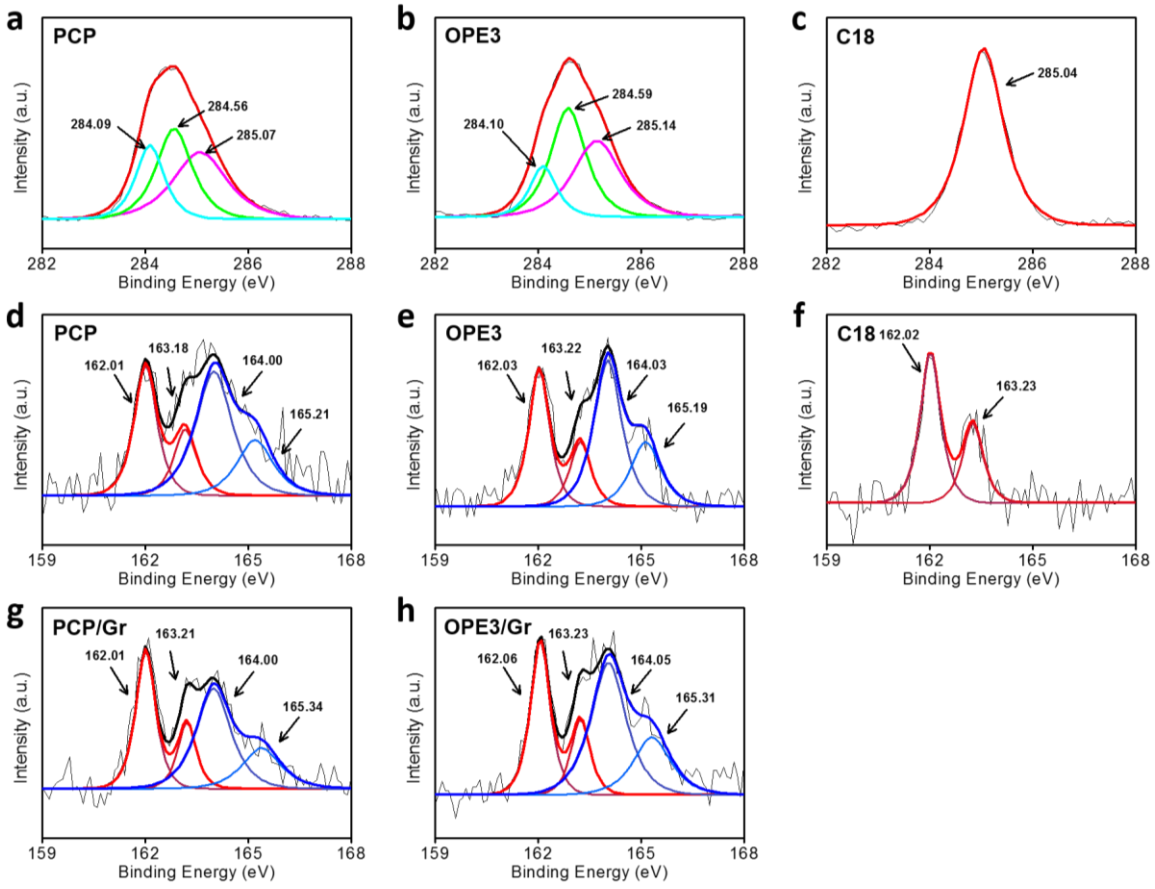

Fig. S3. HR-XPS characterizations. (**A-C**) HR-XPS spectrum of the C (1s) region for PCP (A), OPE3 (B) and C18 (C). (**D-F**) HR-XPS spectrum of the S (2p) region for PCP (D), OPE3 (E) and C18 (F). (**G, H**) HR-XPS spectrum of the S (2p) region for PCP (G) and OPE3 (H) covered with graphene layer.

For the C (1s) region of PCP (fig. S3a), the peak at ~284.09 eV is assigned to alkynyl C (sp); the peak at ~284.56 eV is assigned to C atoms at phenyl; the peak at ~285.07 eV is assigned to C atoms near to C-S bonds. For the C (1s) region of OPE3 (fig. S3b), the peak at ~284.10 eV is assigned to alkynyl C (sp); the peak at ~284.59 eV is assigned to C atoms at phenyl; the peak at

~285.14 eV is assigned to C atoms near to C-S bonds. For the C (1s) region of C18 SAM (fig. S3c), the peak at ~285.04 eV is assigned to alkyl C (sp^3).

For S $2p_{3/2}$, $2p_{1/2}$ doublet in the S (2p) region, two peaks with the same full width at half maximum (FWHM), standard spin-orbit splitting of ~1.2 eV, and a branching ratio ($2p_{3/2}/2p_{1/2}$) of 2 were used for fitting (*23*). Specifically, for the S (2p) region of PCP (fig. S3d), the peaks at ~162.01 eV and ~163.18 eV are assigned to S $2p_{3/2}$ and S $2p_{1/2}$ for the bottom sulfur bound to gold; the peaks at ~164.00 eV and ~165.21 eV are assigned to S $2p_{3/2}$ and S $2p_{1/2}$ for the top free sulfur. As the former sulfur is buried down in the SAM, it is reasonable that the intensity of former peaks is smaller than the intensity of later peaks. Here, these 2 peaks are in a 2:3 ratio, which is a reliable evidence to prove that PCP molecule is successfully assembled on gold film with monolayer (*23*). For the S (2p) region of OPE3 (fig. S3e), similar characteristics can be observed, which indicate the successful fabrication of OPE3 SAM. While, for the S (2p) region of compared 1-Octadecanethiol (C18) SAM, only the peaks from S-Au species can be observed. For the S (2p) region of PCP and OPE3 SAMs covered with graphene layer (fig. S3g,h), the peak characteristics are similar with that of SAMs without graphene layer, which indicate that the top sulfur is still in free state. Therefore, in Au-SAM-graphene structure, there is no apparent chemical bonding between the SAM and graphene.

From intensity ratios of peaks in HRXPS, molecular packing densities and effective thicknesses of the SAMs can be calculated (*23*). For detailed, the C18 SAM was used as a reference, which has a well-defined thickness of 20.9 Å and a molecular density of 4.63×10^{14} cm^{-2}. Based on the S 2p/Au 4f intensity ratio, where only the part of the S (2p) signal related to the Au-S species was used, the molecular packing densities of the SAMs were calculated about 3.19×10^{14} cm^{-2} for PCP and 3.72×10^{14} cm^{-2} for OPE3. Such high packing densities of the SAMs ensure the assembled molecules with high order. Assuming the photoelectron signal with a standard exponential attenuation and using the typical attenuation lengths of densely packed SAMs, based on the C 1s/Au 4f intensity ratio the effective thicknesses of the SAMs were estimated about 14.9 Å for PCP and 16.7 Å for OPE3. Considering the intrinsic molecular length of ~20.6 Å for PCP and OPE3, the molecular tilt angle is 43.4° for PCP and 35.5° for OPE3, which are accordance with the tilt angle ~40° measured from NEXAFS spectra in our previous work for the same SAMs with high order (*23*).

Section S3. Supplementary for theoretical calculations

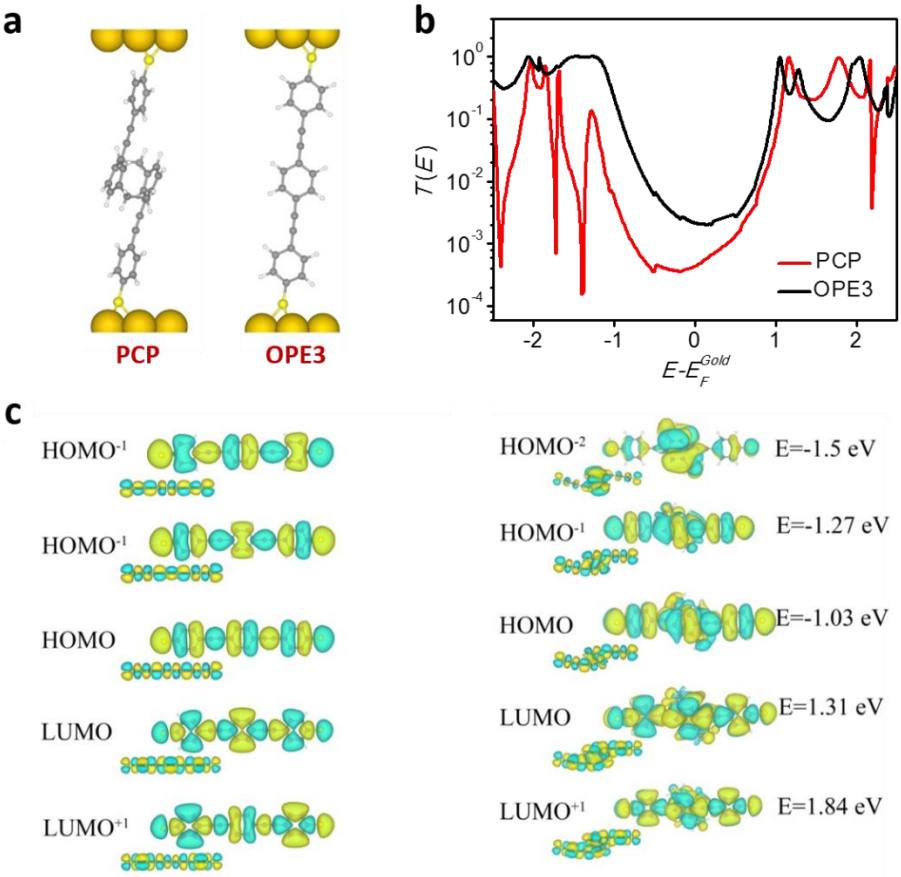

Fig. S4. Supplementary theoretical calculations. (**A**) Schematic illustration of the PCP and OPE3 junctions with gold-gold contact. (**B**) Transmission functions *T*(*E*) for corresponding PCP (red) and OPE3 (black) junctions. (**C**) The Molecular orbitals for OPE3 (left) and PCP (right).

The ratio of the conductance is $\frac{G_{OPE}}{G_{PCP}} = \frac{2.17\times10^{-3}}{4.34\times10^{-4}} = 5$ for OPE3 and PCP with gold-gold contact. These findings are in good agreement with literature (*23, 33*).

Figure S4c shows that for both molecules the inter-orbital quantum interference between eg the HOMO and LUMO is constructive, because their orbital products have opposite signs, as discussed in literature (*24*). However, the broken conjugation of the PCP, which can be regarded as a form of intra-orbital destructive QI between the left and right halves of the molecule, means that there is only a small electronic coupling between the left and right halves of the molecule, which reduces the conductance.

Section S4. Supplementary charge transport in PCP and OPE3 devices

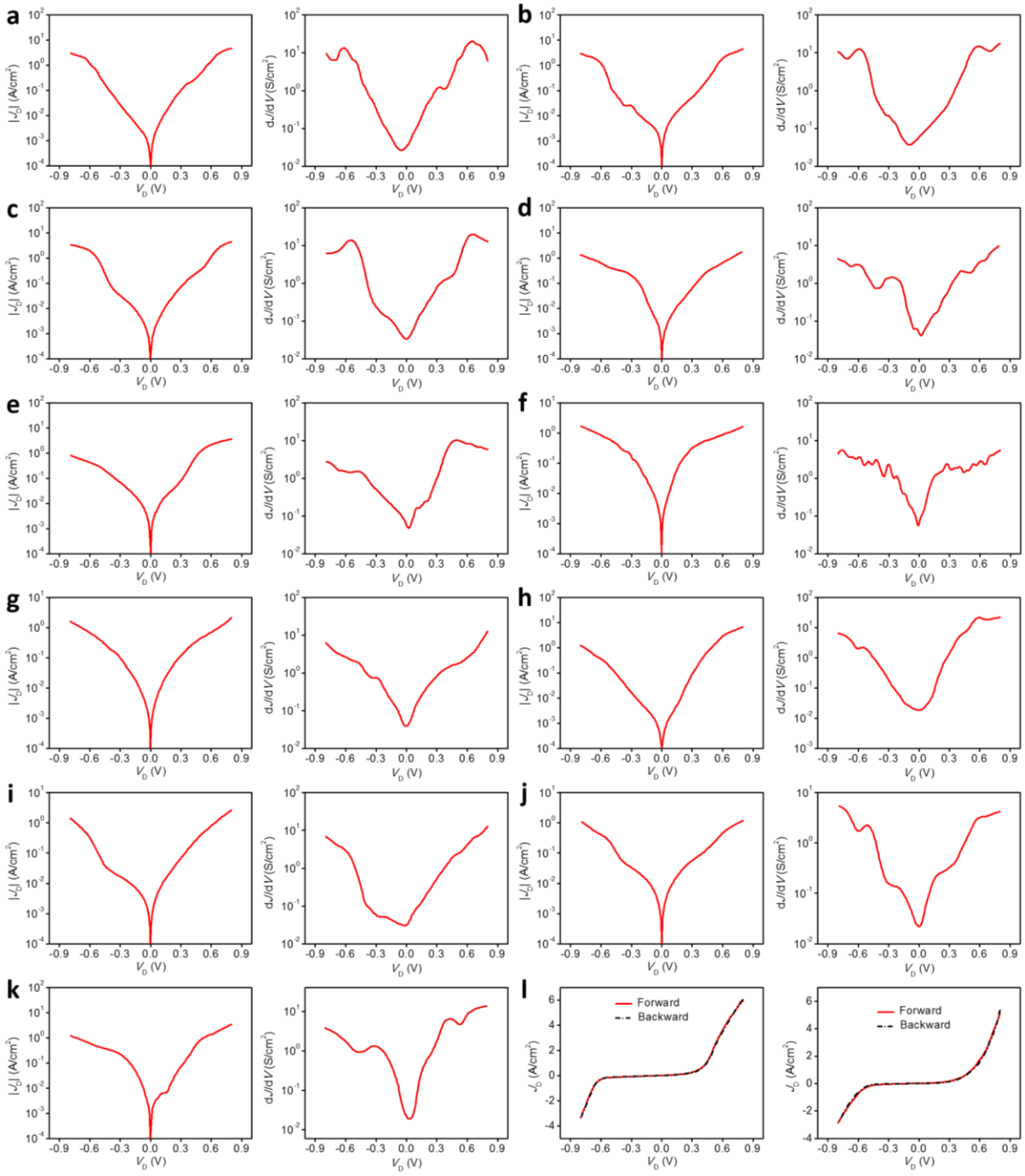

Fig. S5. Charge transport in PCP devices. Current density (J_D) *vs*. bias voltage (V_D) plots (Left) and corresponding differential conductance (dJ/dV) *vs*. V_D plots (Right) for experimental PCP device-2 (**A**), device-3 (**B**), device-4 (**C**), device-5 (**D**), device-6 (**E**), device-7 (**F**), device-8 (**G**), device-9 (**H**), device-10 (**I**), device-11 (**J**) and device-12 (**K**). (**L**) J_D–V_D for two typical devices with forward and backward scan V_D, where no hysteresis can be observed.

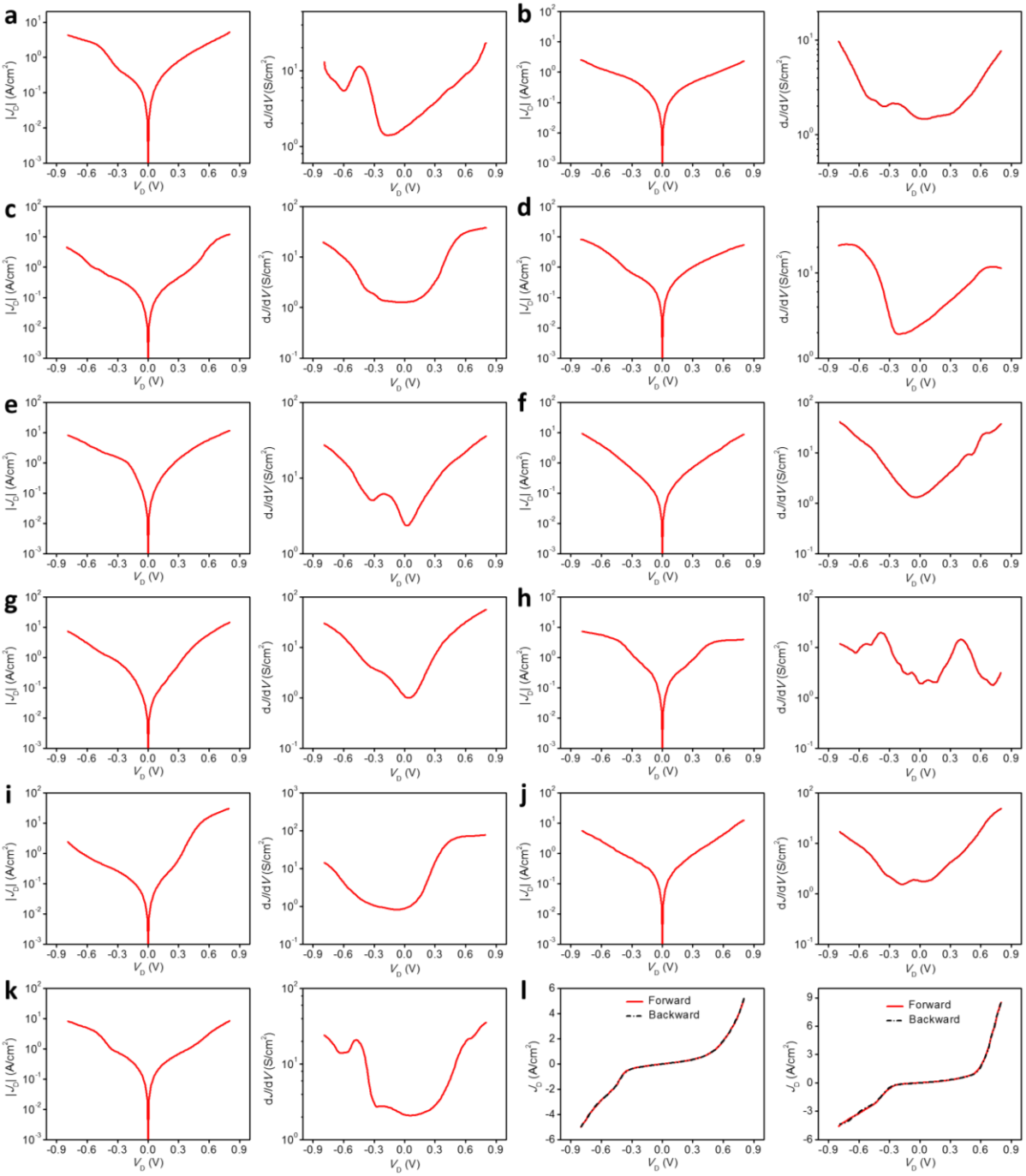

Fig. S6. Charge transport in OPE3 devices. J_D–V_D plots (Left) and corresponding dJ/dV–V_D plots (Right) for experimental OPE3 device-2 (**A**), device-3 (**B**), device-4 (**C**), device-5 (**D**), device-6 (**E**), device-7 (**F**), device-8 (**G**), device-9 (**H**), device-10 (**I**), device-11 (**J**) and device-12 (**K**). (**L**) J_D–V_D for two typical devices with forward and backward scan V_D, where no hysteresis can be observed.

Table S1. Statistic conductance for PCP and OPE3 junctions.

	$G_{VD = 0\ V}$ (S/cm^2)		$G_{VD = 0\ V}$ (S/cm^2)	G_{OPE3}/G_{PCP}
PCP-1	***0.0231***	**OPE3-1**	***1.65***	***71.4***
PCP-2	0.0252	OPE3-2	1.73	
PCP-3	0.0346	OPE3-3	1.47	
PCP-4	0.0318	OPE3-4	1.29	
PCP-5	0.0303	OPE3-5	2.45	
PCP-6	0.0461	OPE3-6	2.51	
PCP-7	0.0513	OPE3-7	1.32	
PCP-8	0.0371	OPE3-8	1.15	
PCP-9	0.0177	OPE3-9	1.94	
PCP-10	0.0272	OPE3-10	0.93	
PCP-11	0.0205	OPE3-11	1.78	
PCP-12	0.0185	OPE3-12	2.13	
PCP-*Exp*	**0.0303 ± 0.0106**	**OPE3-*Exp***	**1.70 ± 0.49**	**56.1**
PCP-*Cal*	**0.0102 nS**	**OPE3-*Cal***	**0.664 nS**	**65.1**

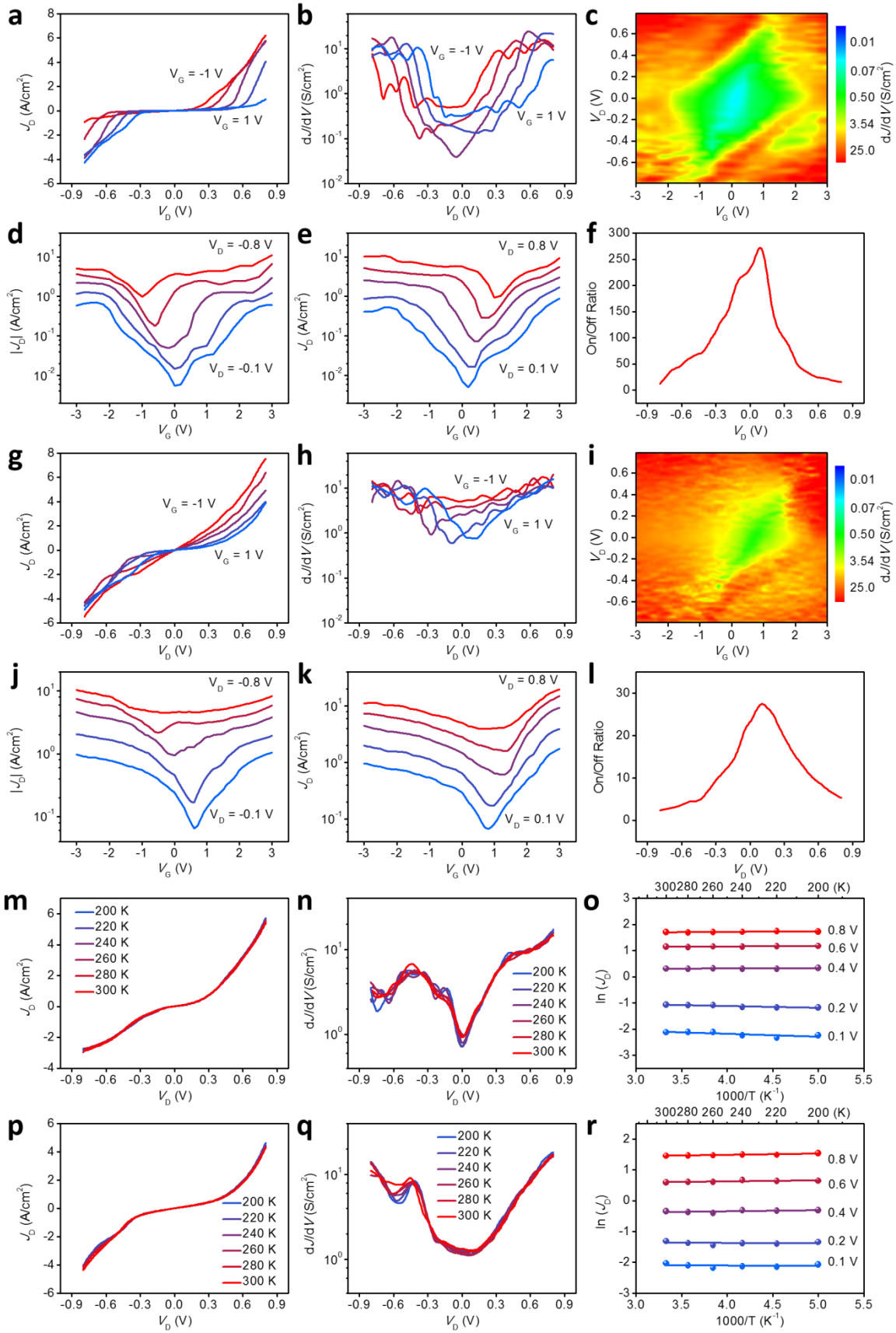

Fig. S7. Temperature-dependent performances for PCP and OPE3. (**A, B**) J_D–V_D (A) and dJ/dV–V_D (B) curves for PCP with V_G varying from –1 to 1 V with step of 0.5 V. (**C**) Two-dimensional visualization of dJ/dV plotted *vs.* V_G and V_D for PCP. (**D, E**) Transfer characteristics for PCP with V_D = –0.1, –0.2, –0.4, –0.6, –0.8 V (D) and V_D = 0.1, 0.2, 0.4, 0.6, 0.8 V (E). (**F**) V_D

dependent on–off ratio for PCP. (**G, H**) J_D–V_D (G) and dJ/dV–V_D (H) curves for OPE3 with V_G varying from –1 to 1 V with step of 0.5 V. (**I**) Two-dimensional visualization of dJ/dV plotted *vs*. V_G and V_D for OPE3. (**J, K**) Transfer characteristics for OPE3 with V_D = –0.1, –0.2, –0.4, –0.6, –0.8 V (J) and V_D = 0.1, 0.2, 0.4, 0.6, 0.8 V (**K**). (**L**) V_D dependent on–off ratio for OPE3. All data in **a–l** is measured at room temperature. (**M, N**) J_D–V_D (M) and dJ/dV–V_D (N) curves for PCP at V_G = 0 V with temperature varying from 200 to 300 K. (**O**) Arrhenius plots of ln (J_D) *vs*. 1/T for PCP at V_D = 0.1, 0.2, 0.4, 0.6, 0.8 V. (**P, Q**) J_D–V_D (P) and dJ/dV–V_D (Q) curves for OPE3 at V_G = 0 V with temperature varying from 200 to 300 K. **r,** Arrhenius plots of ln (J_D) *vs*. 1/T for OPE3 at V_D = 0.1, 0.2, 0.4, 0.6, 0.8 V.

For PCP and OPE3 devices measured at room temperature (298 K), the gate performances (fig. S7a–l) are nearly the same as that measured at 200 K (Figs. 4 and 5). Therefore, the fabricated vertical molecular transistors can stably operate at room temperature. Although the room temperature data are similar to the data at 200 K, they still have some differences. For instance, due to thermal fluctuation effect, a dash of noise happens for the devices measured at 298 K, which leads that two-dimensional visualizations of dJ/dV have more complex structures at 298 K (figs. S7c,i) than at 200 K (Fig. 4C,F). Furthermore, the maximum on–off ratio decreases from ~320 at 200 K (fig. S8g) to ~280 at room temperature (fig. S7f) for PCP and from ~33 at 200 K (fig. S8g) to ~29 at room temperature (fig. S7l) for OPE3, thus the maximum on–off ratio for PCP is about one order of magnitude higher than that for OPE3 at both 200 K and room temperature. For the temperature dependent performances, it can be observed from dJ/dV–V_D curves (fig. S7n,q) that the peaks and edges are broadening and the valleys are lifting with temperature increasing from 200 to 300 K, which indicate the thermal effects on the charge transports. Furthermore, Arrhenius plots of ln (J_D) *vs*. 1/T for PCP and OPE3 at different V_D show nearly horizontal characteristics, which imply the temperature-independent coherent tunneling transport through the junctions without charging energies (*34*).

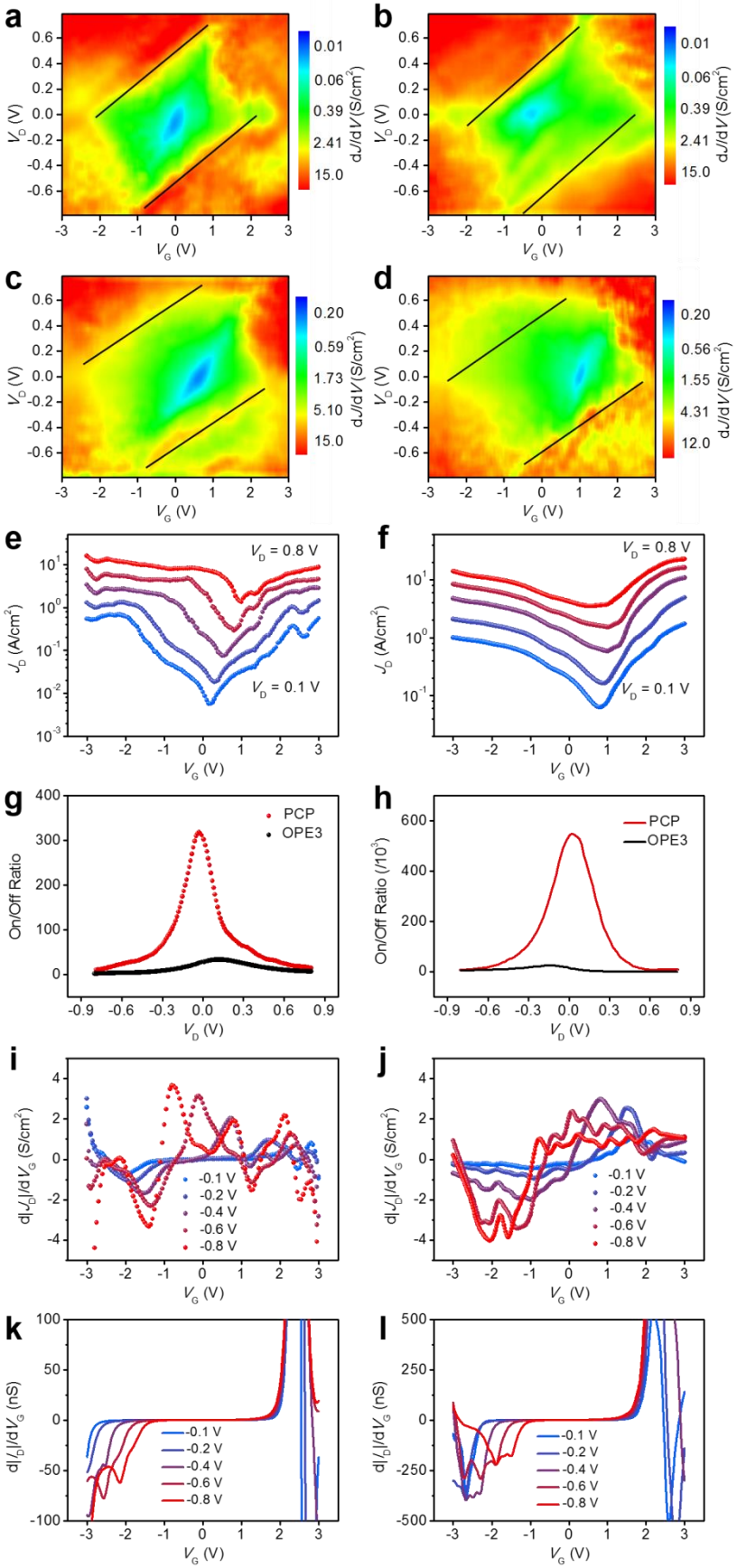

Fig. S8. Supplementary gate performances for PCP and OPE3 transistors. (**A, B**) Two-dimensional visualization of d*J*/d*V* plotted *vs.* V_G and V_D for another two PCP devices. (**C, D**) Two-dimensional visualization of d*J*/d*V* plotted *vs.* V_G and V_D for another two OPE3 devices. The

black lines in (A–D) are auxiliary markers of corresponding conductance diamond edges. (**E**) Experimental transfer characteristics for PCP. (**F**) Experimental transfer characteristics for OPE3. V_D is varied from 0.1, 0.2, 0.4, 0.6 to 0.8 V in (E, F). (**G**) Compared V_D dependent on–off ratio for experimental PCP and OPE3. (**H**) Theoretical V_D dependent on–off ratio for PCP and OPE3. (**I, J**) Experimental $d|J_D|/dV_G–V_G$ for PCP (I) and OPE3 (J). (**K ,L**) Theoretical $d|I_D|/dV_G–V_G$ for PCP (K) and OPE3 (L). V_D is varied from –0.1, –0.2, –0.4, –0.6 to –0.8 V in fig. S8i–l.

The V_G/V_D slopes of marked conductance diamond edges for PCP are 0.2446 (fig. S8a) and 0.2619 (fig. S8b); the slopes of conductance diamond edges for OPE3 are 0.1981 (fig. S8c) and 0.2062 (fig. S8d). These slope values are close to the values shown in Fig. 4C,F of 0.2493 for PCP and 0.2095 for OPE3, which indicate that these values are robust across different devices.

From fig. S8i–l, it can be observed that the V_D dependent moving directions for the experimental and theoretical peaks of dI/dVs are similar with each other. Especially, the peaks of dJ/dVs and dI/dVs at negative V_G move along the positive V_G axis with V_D varying from –0.1 to –0.8 V, which are accordant with the shrinking valleys shown in Fig. 5.

Section S5. The performances for compared devices

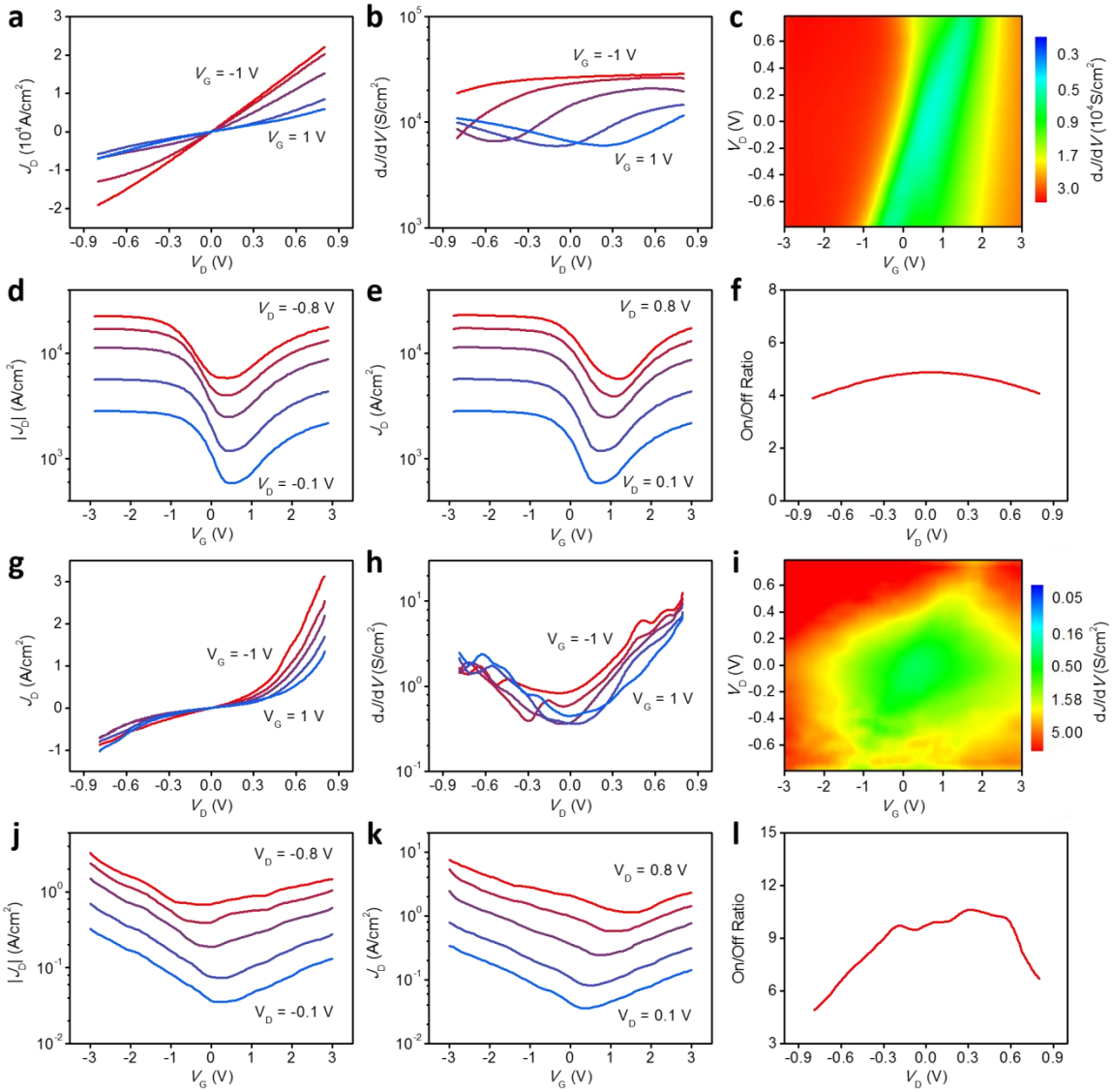

Fig. S9. Gate performances for compared graphene and C18 devices. (**A, B**), J_D-V_D characteristics (A) and dJ/dV-V_D characteristics (B) for graphene device with V_G changing from -1 to 1 V at step of 0.5 V. (**C**) Two-dimensional visualization of dJ/dV plotted *vs.* V_G and V_D for graphene device. (**D, E**) Experimental transfer characteristics for graphene device at V_D = –0.1, –0.2, –0.4, –0.6 and –0.8 V (D) and V_D = 0.1, 0.2, 0.4, 0.6 and 0.8 V (E). (**F**) Corresponding V_D dependent on–off ratio for graphene device. (**G, H**) J_D-V_D characteristics (G) and dJ/dV-V_D characteristics (H) for C18 device with V_G changing from -1 to 1 V at step of 0.5 V. (**I**) Two-dimensional visualization of dJ/dV plotted *vs.* V_G and V_D for C18 device. (**J, K**) Experimental transfer characteristics for C18 device at V_D = –0.1, –0.2, –0.4, –0.6, –0.8 V (J) and V_D = 0.1, 0.2, 0.4, 0.6, 0.8 V (K). (**L**) Corresponding V_D dependent on–off ratio for C18 device.

The control C18 device (fig. S9g–l) shows a similar field-effect behavior as PCP and OPE3 devices (Figs. 4,5 and fig. S8), but with poor gate performance. For instance, the highest on–off ratio for C18 is ~10 (fig. S9l), which is much less than that of ~320 for PCP and ~34 for OPE3 (fig. S8g).